Meccanica (2023) 58:1823–1847
https://doi.org/10.1007/s11012-023-01700-2

Research on frictional characteristics of a space split telescope deployable mechanism variable diameter internal drive device in the inter-stage transition phase

Yingjun Guan · Weiqi Huang · Hao Wang · Huanquan Lu · Huisheng Yang

Received: 21 May 2023 / Accepted: 16 August 2023 / Published online: 26 August 2023

Abstract In order to enhance the spreading and retracting capability of the variable diameter internal drive device in the inter-stage transition phase of the space telescope deployable mechanism, this paper investigates the friction characteristics of the device at different moments during this phase based on the elastic Hertzian contact model. Firstly, the elastic contact state and friction type of the variable diameter internal drive device are analyzed at different moments during the transition stage. Next, a mechanical model is constructed to describe the relationship between the friction factor and radial preload in the inter-stage transition stage. Then, the force state in the inter-stage transition stage is analyzed using the finite element method. Finally, a test prototype is established to verify the elastic contact friction state of the variable diameter internal drive device during the inter-stage transition stage. The results indicate that the contact area between the radial preload and the elastic material of the variable diameter internal drive device has a significant impact on the friction characteristics during the inter-stage transition phase. Therefore, the friction factor at different moments during the inter-stage transition phase can be effectively adjusted by utilizing the radial load, thus enhancing the stability of the variable diameter internal drive device during the inter-stage transition.

Keywords Deployable mechanism · Spreading and retracting capability · Variable diameter internal drive device · Inter-stage transition · Elastic contact friction

1 Introduction

The space deployable mechanism is an essential component of space telescopes, extensively utilized in the aerospace field. Due to the superior capability of space-based telescopes in exploring distant space compared to their ground-based counterparts, the aperture requirements for space-based telescopes have increased. However, large-aperture space telescopes face significant volume constraints due to the limited internal space within rocket fairings. Therefore, space deployable mechanisms are typically employed to enable the transition from a compact stowed state to a fully deployed state for large-aperture space telescopes [1–6]. Over the past few decades, various driving techniques, including hinged structures [7], thin-walled tubes, bellows, and rollable systems [8, 9], have been utilized to enhance the deployment capability of space deployable mechanisms. The

Y. Guan · W. Huang · H. Wang · H. Lu
Changchun University of Technology, College of Electrical and Mechanical Engineering,, Changchun 130012, Jilin, China

H. Yang (✉)
Changchun Institute of Optics and Precision Mechanics and Physics, Chinese Academy of Sciences, Changchun 130033, Jilin, China
e-mail: ciomp_yhsh@126.com

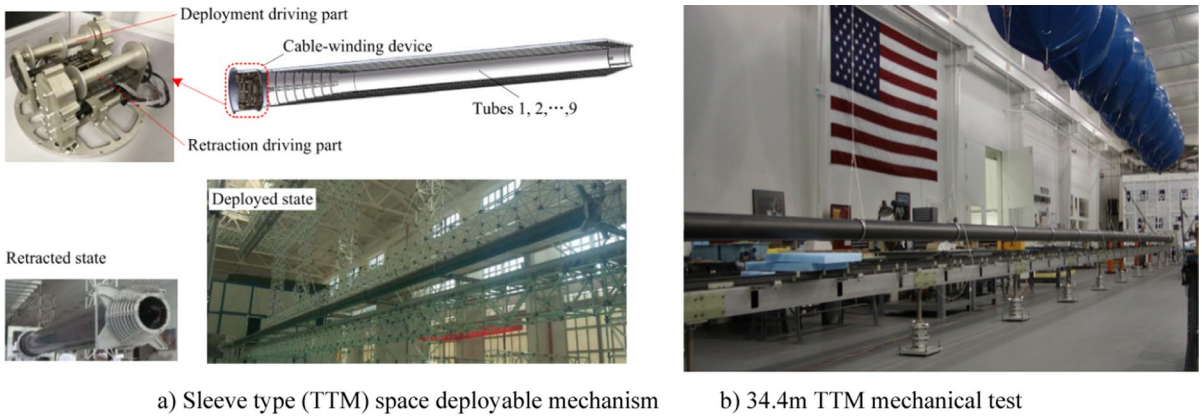

a) Sleeve type (TTM) space deployable mechanism b) 34.4m TTM mechanical test

Fig. 1 Schematic diagram of TTM deployable mechanism and field test

deployment configuration of large-aperture space telescopes shares similarities with truss-based deployable antenna structures, characterized by high stiffness, strong extensibility, and high foldability. Recent studies by Jinwei Guo's team have utilized tetrahedral elements [10] and hexagonal deployable units [11] for antenna structure analysis and design, ensuring dynamic characteristic analysis and practical applications of parallel truss antenna structures through dynamic modeling and vibration analysis [12]. Furthermore, their research on truss-based deployable antenna structures provides valuable insights into the conceptualization of deployable mechanisms in large-aperture telescopes. Unlike other dimensional forms, the bellows-type deployable mechanism exhibits higher deployment precision, stiffness, and strength from a practical application perspective. Additionally, it offers advantages such as a small radial compact size, stable deployment process, simple structure, and high reliability, as illustrated in Fig. 1a.

The US company Northrop Grumman conducted extensive research on the Telescopic Tube Mast (TTM) developed for the Inflatable Sunshield In Space (ISIS) system. They achieved a fully extended length of 6.70 m [13]. In a separate study, Mehran Mobrem and colleagues performed a mechanical analysis of the TTM's expansion and contraction. They conducted test analysis on a 34.4 m TTM designed for terrestrial applications, as shown in Fig. 1b, and found that the stiffness and frequencies of the TTM were more suitable for space applications compared to other space deployable mechanisms [14]. Another research team, led by Nailiang Cao, focused on the TTM within the sunshield deployment mechanism of space telescopes. They simulated the TTM's structural state under axial loads in space and observed stable movement under a 30N axial load for an 8 m TTM [15]. However, traditional TTM systems suffer from limitations in their driving method, resulting in short deployment distances and heavy weights [16–18]. To address this, a three-dimensional structure called the variable diameter internal drive device (Fig. 2) enables progressive deployment of the tube with a smaller mass. It ensures the mechanical performance of the tube while maximizing its extended deployment distance. Nonetheless, effectively transitioning the non-continuous surfaces between stages inside the tube remains a pressing technical challenge.

In recent years, scholars have extensively analyzed the motion characteristics between different materials during inter-stage transitions and identified the mechanical properties of viscoelastic materials and metal materials as the primary factors influencing inter-stage transition capability. Paul Wagner conducted a study on the frictional contact between rubber wheels and rough road surfaces. By employing multiscale numerical simulations that consider hysteresis and adhesion effects, he discovered deviations in the frictional contact of viscoelastic materials from traditional mechanical theories [19]. Laura De Lorenzis and her colleagues investigated the contact between viscoelastic rubber materials and metal surfaces. They developed a frictional contact model for different roughness levels of metal surfaces and rubber, revealing a correlation between the contact area and the Asperity between the materials [20]. Furthermore, Fangman Xu and his colleagues further explored the relationship between

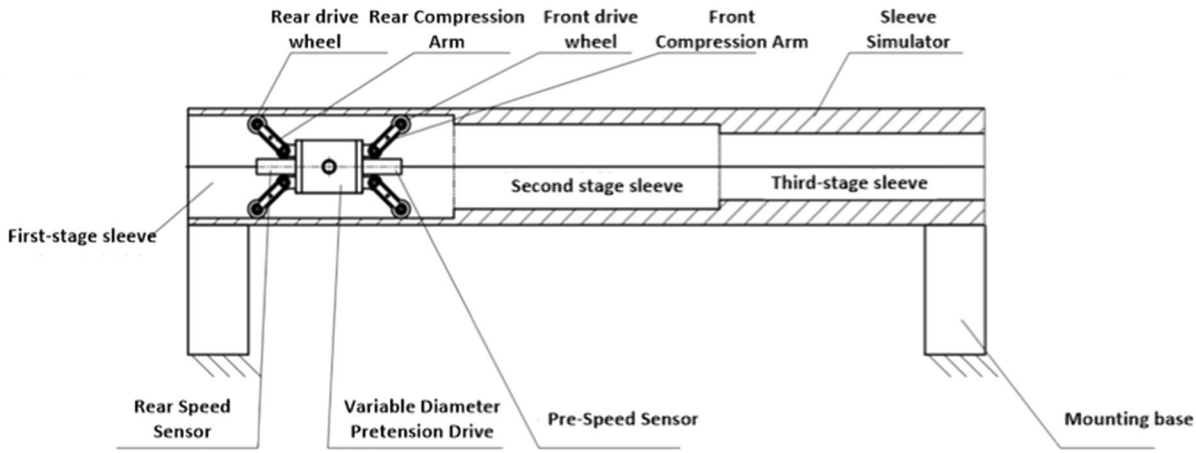

Fig. 2 Schematic diagram of the variable diameter internal drive device in TTM

frictional contact types and contact areas using friction contact models with varying levels of roughness and rubber. Their hypothesis was validated through sliding friction experiments [21]. Liang and his team experimentally verified the relationship between frictional contact of viscoelastic materials and the contact area between the two materials. They observed a consistent linear relationship between frictional force and normal load, with the relationship between frictional force and contact area remaining linear only during the loading stage [22]. Valentin L. Popov and his colleagues investigated the influence of friction coefficients by considering the maximum and minimum scales of contact body roughness between the two materials. Utilizing a simplified one-dimensional model, they uncovered that surfaces often exhibit significant surface gradients at smaller scales, indicating that the minimum scale exerts the greatest influence on friction coefficients. They also discovered that normal contact has a certain impact on friction coefficients [23].

To ensure the effective inter-stage transition of the variable diameter internal drive device on the inner surface of the tube, it is crucial to consider the motion characteristics between the viscoelastic rubber wheel and the metal surface. Additionally, establishing an elastic contact friction model under different motion states is necessary. By analyzing the relationship between fitting and radial preload, the goal of achieving effective inter-stage transition under load conditions can be attained. The organization of the remaining sections in this paper is as follows. In Sect. 2, we introduce the internal working state of the variable diameter internal drive device in the tube-like deployable boom. An analysis of elastic contact friction is conducted for the different stages of inter-stage transition on the inner wall of the tube, and mathematical models are established to fit the relationship between radial preload and elastic contact friction at each stage. In Sect. 3, a simulation analysis is performed to examine the transition state of the variable diameter internal drive device on the non-continuous surface of the tube's inner wall, aiming to verify the accuracy of the elastic contact friction theory. Section 4 focuses on the design and manufacture of a prototype, followed by deployment experiments to validate the effectiveness of the inter-stage transition and the correctness of the elastic contact friction status in each stage. Finally, Sect. 5 concludes the entire paper and outlines the scope of future work.

2 Method and data fitting

2.1 Analysis of the transition state between stages of variable diameter internal drive devices

In the space environment, the tube-type space deployable mechanism undergoes axial expansion and contraction to adapt to the changing working conditions of its carrier. Therefore, replacing the traditional tube drive mechanism with a variable diameter internal drive device is advantageous in maximizing the deployment distance and load capacity. The variable diameter internal drive device offers a simple

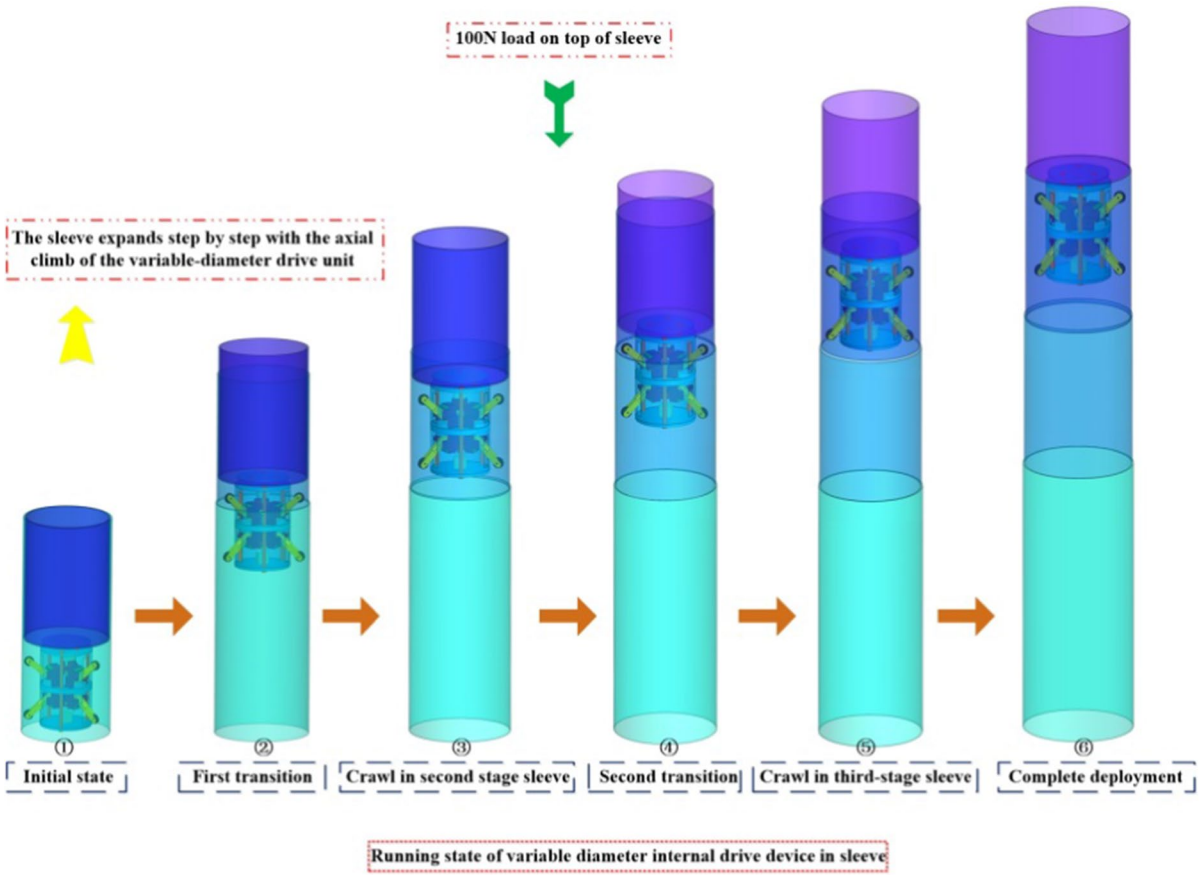

Fig. 3 Variation diameter internal drives inside the sleeve for unfolding work schematic

structure, small mass, and high precision, enabling better axial expansion and contraction of the tube.

The motion of the variable diameter internal drive device inside the tube is divided into six stages: initial compression state ①, first-stage inter-stage transition ②, transition of the continuous inner surface of the second-stage tube ③, second-stage inter-stage transition ④, transition of the continuous inner surface of the third-stage tube ⑤, and full expansion of the fourth-stage tube ⑥, as shown in Fig. 3. During the axial expansion of each stage using the variable diameter internal drive device, a constant load of 100N is applied to the fourth-stage tube to simulate the load conditions during operation.

The inner surface of the tube deployable mechanism can be classified into continuous and non-continuous surfaces. Each stage tube is an independent structure, resulting in a continuous inner surface for each stage tube. However, during the continuous expansion of the stages, the inner surface of the inter-stage tubes presents a stepped non-continuous surface. These non-continuous surfaces, combined with the varying diameters of the stage tubes, can lead to issues such as rubber wheel slipping, jamming, and sliding during the inter-stage transition. Therefore, the variable diameter internal drive device is employed to enable real-time adjustment of the radial preload and driving load applied to the rubber wheel (Fig. 4).

During the transition phase between stages, the variable diameter internal drive device encounters non-continuous surfaces. The driving wheel, which is made of rubber material, exhibits a nonlinear motion during this transition phase due to the viscoelastic properties of rubber, as illustrated in Fig. 5.

The entire process consists of six stages. Stages ④ and the final ⑥ are the same, as they involve movement on the same continuous surface but with different inner wall diameters of the tube. In Stage ①, the

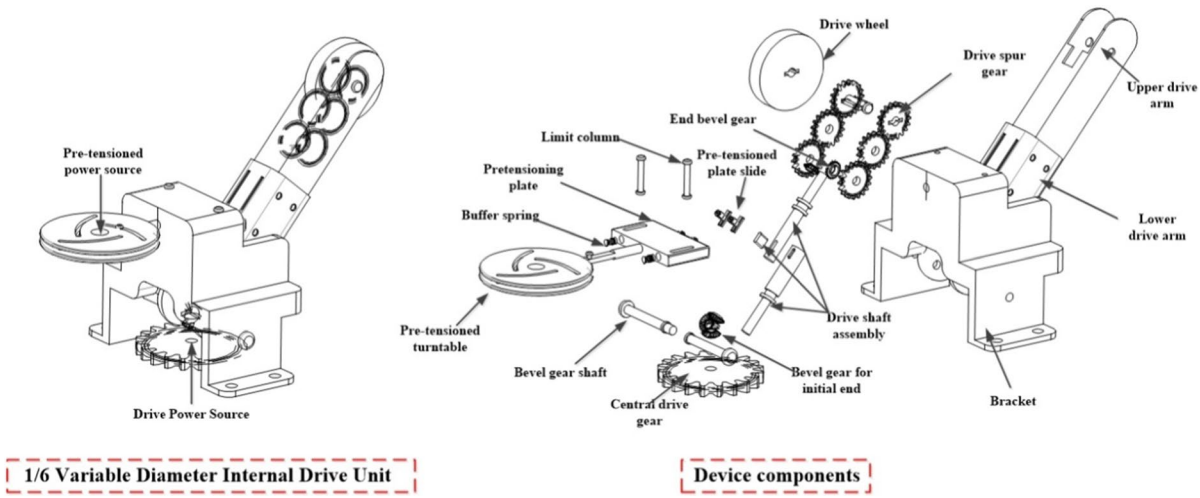

Fig. 4 1/6 Structure of reducer internal drive to achieve preload, reducer and drive capability

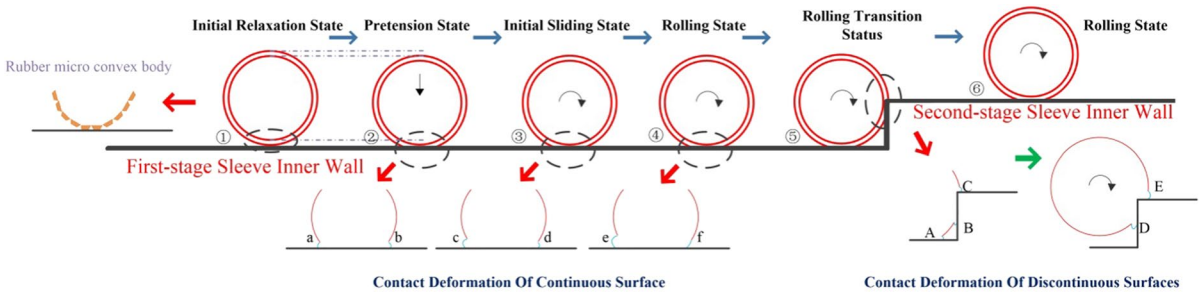

Fig. 5 Schematic diagram of the motion analysis of the drive wheel transition stage

rubber wheel is not subjected to any external forces. Stage ② represents the maximum static friction stage, where the rubber wheel experiences radial preload to achieve maximum static friction with the inner wall of the tube. At this stage, localized regions a and b demonstrate compression of the rubber, resulting in shape deformation due to its elastic nature, which is the main focus of our study on elastic contact behavior. Stage ③ is the sliding stage, where sliding occurs within the compressed contact area based on the maximum static friction achieved in Stage ②. Localized regions c and d illustrate this behavior, with region d starting to compress and region c starting to stretch. Stages ④ and ⑥ are rolling stages on the same surface. The rubber wheel rolls and expands on this continuous surface under the combined action of the driving force and radial preload. Since each section of the tube has a different diameter, the applied radial preload varies. As a result, localized regions e and f display different compression and stretching states in each stage. Notably, the compression at region f and the stretching at region e gradually increase.

Stage ⑤ involves the unfolding of the non-continuous surface, during which the variable diameter internal drive device undergoes axial expansion and the rubber wheel transitions on the non-continuous surface. When the rubber wheel initially contacts the non-continuous surface, contact changes occur at regions A, B, and C. Further changes occur at regions C and D during the transitional phase of the rubber wheel.

2.2 Transition elastic contact friction analysis between stages of variable diameter internal drive devices

2.2.1 Elastic contact friction type

Regarding the motion state of the rubber wheel structure of the variable-diameter internal drive device during the unfolding process on both discontinuous and continuous surfaces in the axial direction, as well as the six stages of motion, a clearer elucidation of the frictional contact types between the rubber wheel and the inner wall of the metal sleeve is provided. The complete motion is divided into four types of frictional contact, namely maximum static friction, elastic sliding contact friction, elastic rolling contact friction, and viscoelastic contact friction. Among these types, the elastic rolling contact friction is further classified into the steady rolling stage and the transitional rolling stage.

During the initial stage and the stage of applying radial pre-tightening force, represented by stages ① and ② in Fig. 5, the maximum static friction occurs between the rubber wheel and the inner wall of the metal sleeve. This friction is a result of the radial pressure that compresses the rubber wheel system against the inner wall of the sleeve. The deformed area of the rubber on the inner wall of the sleeve due to compression can be calculated as follows:

$$A_T = A_0\left(p/E'\right)^{2/3} \tag{1}$$

where A_T is the apparent area of contact, and A_0 is a constant, and E is the modulus of elasticity of the rubber, and p is the contact pressure (Further to obtain the friction force in the static friction phase).

$$F = KA_T \tag{2}$$

where K is a constant related to velocity, temperature and two pairs of friction surfaces, generally $K=2$. Further to obtain the friction coefficient:

$$\mu = \mu_0\left(p/p_0\right)^{-1/3} \tag{3}$$

where p_0 is the contact center pressure; μ_0 is the reference value of friction coefficient of rubber, generally 0.41.

In stage ③ is the elastic sliding contact friction state, at this time it is necessary to consider the pressure and contact radius of the center of the contact area of the rubber wheel in relation to the normal force, as shown in Fig. 6.

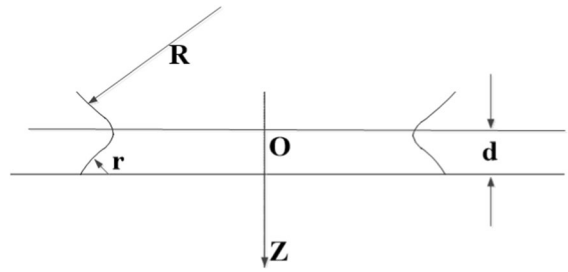

Fig. 6 Contact between elastic wheel body and rigid surface in sliding phase

Firstly, the pressure distribution is obtained according to Hertzian contact theory p, vertical displacement u_z and the total force Fz. The displacement of a flexible wheel at a contact point on a rigid surface is equal to.

$$u_z = d - \frac{r^2}{2R} \tag{4}$$

Equation change through the vertical displacement with the displacement of the contact point to obtain the real generated displacement a and p_0:

$$\frac{1}{E^*}\frac{\pi p_0}{4a}\left(2a^2 - r^2\right) = d - \frac{r^2}{2R} \tag{5}$$

Contact radius at this point and maximum pressure at this point:

$$a^2 = Rd \tag{6}$$

$$p_0 = \frac{2}{\pi}E^*\left(\frac{d}{R}\right)^{1/2} \tag{7}$$

Bringing Eqs. (6) and (7) into the total force Fz in, we can obtain the normal force as.

$$F = \frac{4}{3}E^*R^{1/2}d^{3/2} \tag{8}$$

Further obtain the pressure at the center of the contact area and the contact radius versus the normal force:

$$p_0 = \left(\frac{6FE^{*2}}{\pi^3R^2}\right)^{1/3},\ a = \left(\frac{3FR}{4E^*}\right)^{1/3} \tag{9}$$

In sliding contact friction, the sliding friction coefficient is calculated by the formula.

$$\mu_f = \frac{F_R}{F_n} \tag{10}$$

where F_n is the total normal force acting uniformly on the macroscopic region A between the sliding body and the surface. F_R is the energy loss from material deformation to obtain the frictional force.

In calculating the deformation and energy loss in a high elastomer, the average contact area of a micro-convex body is $\Delta A \approx Rl$, then the characteristic diameter of a micro contact:

$$r \approx \sqrt{\Delta A} \approx \sqrt{RL} \tag{11}$$

An object with velocity V sliding over a distance of characteristic size r the time taken to travel the distance of $t \approx \frac{r}{V} \approx \frac{\sqrt{Rl}}{V}$, where $k \approx 2$. The effective modulus of elasticity of the rubber:

$$E^* = \frac{E}{1-\nu^2} = \frac{2(1+\nu)G}{1-\nu^2} \approx 4G \tag{12}$$

where G is the shear modulus and ν is the Poisson's ratio. Since the shear modulus is frequency dependent, the $\tilde{\omega} \approx \frac{1}{t} \approx \frac{v}{r}$ characteristic frequency is substituted into the average pressure $\langle \sigma \rangle = \frac{F_N}{A} = \kappa^{-1} E^* \nabla z$ in, i.e.: $\langle \sigma \rangle = 4\kappa^{-1} \left| \hat{G}(\tilde{\omega}) \right| \nabla z$. Calculate the energy loss per unit volume of the microscopic contact:

$$G''(\tilde{\omega}) = \frac{2\overline{P}|\hat{G}(\tilde{\omega})|^2}{\tilde{\omega}\langle \sigma \rangle^2} \tag{13}$$

Multiply with the depth r of the deformation volume, at this time the depth r with the vertical displacement, the frictional force through the energy loss generated by the deformation is calculated by the formula.

$$F_R = \frac{1}{2}\tilde{\omega}\langle \sigma \rangle^2 \frac{G''(\tilde{\omega})}{|\hat{G}(\tilde{\omega})|^2} * \frac{\pi p_0}{4E^* a}\left(2a^2 - r^2\right) \tag{14}$$

where $\hat{G}(\tilde{\omega})$ is the complex shear modulus; $G''(\tilde{\omega})$ is the loss modulus. The final sliding friction coefficient is obtained as.

$$\mu = \frac{1}{2}\tilde{\omega}\langle \sigma \rangle^2 \frac{G''(\tilde{\omega})}{|\hat{G}(\tilde{\omega})|^2} * \frac{\pi p_0}{4E^* a}\left(2a^2 - r^2\right) / \frac{4}{3} E^* R^{1/2} d^{3/2} \tag{15}$$

In stage ④, which represents the phase of elastic rolling contact friction, it corresponds to the steady rolling stage. Within the steady rolling domain, the wheel exhibits an adhesion zone at the leading edge and a sliding zone at the trailing edge. The presence of the sliding zone results in a deviation between the rolling wheel's velocity and the circumferential speed, known as the slip velocity. This slip is induced by the elastic deformation of the wheel, as illustrated in Fig. 7.

The wheel system goes through elastic rotation and rigid rotation, so the circumferential speed of the wheel is greater than the moving speed, but for the brake wheel, the circumferential speed is less than the moving speed. Therefore, the speed difference $v_{\text{creep}} = v - \Omega R$ is proportional to the moving speed v, which is expressed in dimensionless terms in order to describe the characteristics of crawling, i.e.: $s = \frac{v-\Omega R}{v} = 1 - \frac{\Omega R}{v}$, where is called s is the slip ratio. The slip ratio is equal to the strain in the contact adhesion zone $\mathcal{E}_{xx}$, the material density of the adhesion zone $\rho_0/\left(1+\varepsilon_{xx}\right)$, the speed of contact surface movement is v, and the mass flow density of the contact area is $v\rho_0/\left(1+\varepsilon_{xx}\right)$. The slip ratio at this point:

$$s = \frac{\varepsilon_{xx}}{1+\varepsilon_{xx}} \approx \varepsilon_{xx} \tag{16}$$

The tangential force is obtained through the theory of elasticity mechanics, as shown in Fig. 8.

$$\tau(r) = \sigma_{xr}(r) = \tau_0 \sqrt{1 - r^2/a^2} \tag{17}$$

Acting on the circular surface, the resulting tangential displacement is.

$$u_x = \frac{\pi \tau_0}{32Ga}\left[4(2-\nu)a^2 - (4-3\nu)x^2 - (4-\nu)y^2\right] \tag{18}$$

Stress distribution and the displacement resulting from this stress acting in a band of width $2a$:

$$\tau = \sigma_{zx}(x) = \tau_0 \sqrt{1 - x^2/a^2} \tag{19}$$

$$u_x = \text{ Constant} - \tau_0 \frac{x^2}{aE^x} \tag{20}$$

The pressure distribution of the total contact can be obtained from the Hertzian expression:

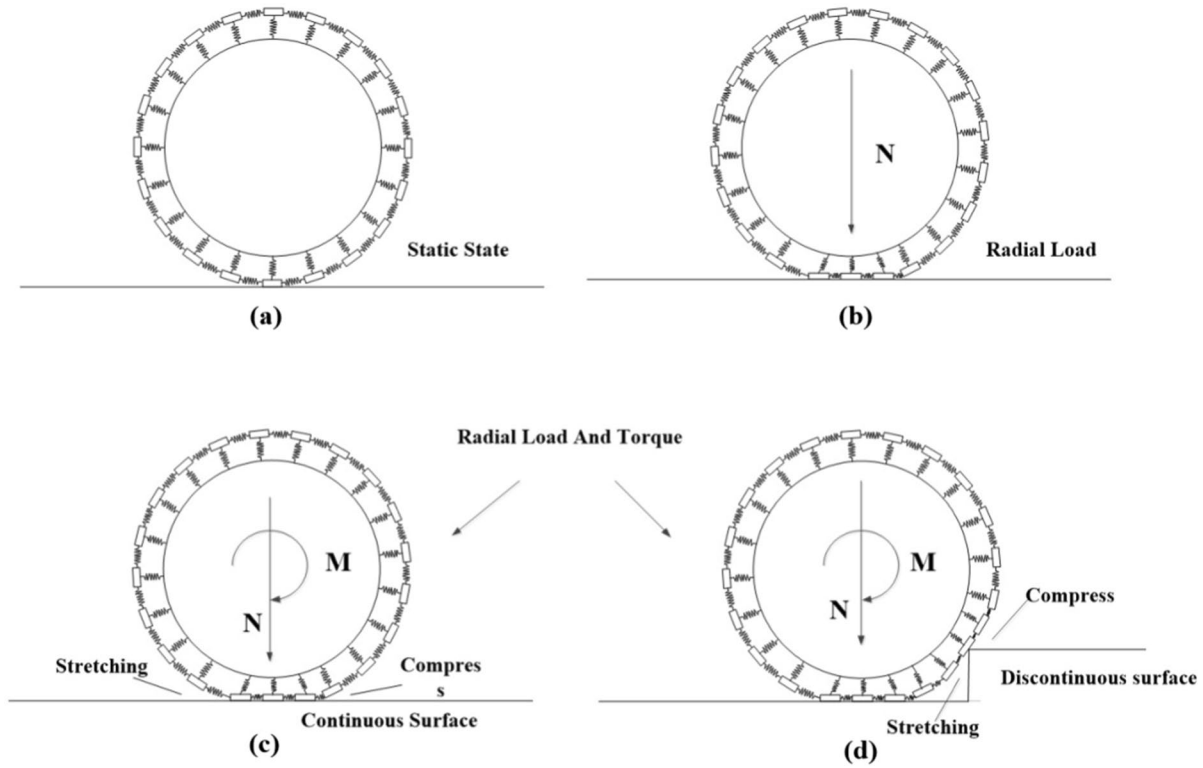

Fig. 7 Simplified model of elastic wheel surface under traction force

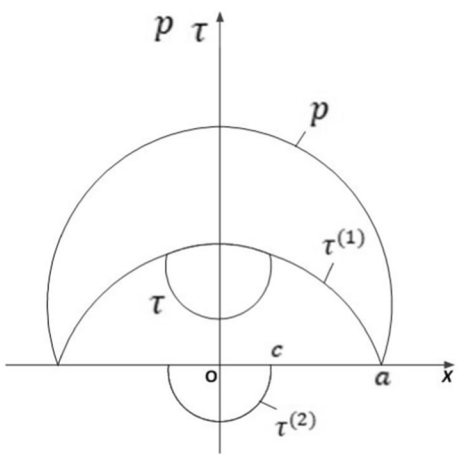

Fig. 8 Normal and tangential stresses in tangential contact

$p(x) = p_0\left(1 - \frac{x^2}{a^2}\right)^{\frac{1}{2}}$. In the complete sliding zone, the smooth rolling contact condition must satisfy $\tau(x) = \mu p(x)$.

In response to the $\tau = \tau^{(1)}(x) + \tau^{(2)}(x)$ stress distribution, the two conditions that need to be satisfied, stress $\tau^{(1)}(x)$ and $\tau^{(2)}(x)$ the displacements due to the stresses are equal $u_x^{(1)} = C^{(1)} - \tau_1 \frac{x^2}{aE^*}$ and $u_x^{(2)} = C^{(2)} +_{\tau_2} \frac{(x-d)^2}{cE^*}$, then the total displacements and strains are:

$$u_x = \text{Constant} - \tau_1 \frac{x^2}{aE^*} + \tau_2 \frac{(x-d)^2}{cE^*} \tag{21}$$

$$\frac{\partial u_x}{\partial x} = -\tau_1 \frac{2x}{aE^*} + \tau_2 \frac{2(x-d)}{cE^*} \tag{22}$$

To satisfy the first condition above, in the adhesion zone, the deformation is constant and there must be $\tau_2 = \frac{c}{a}\tau_1$, according to $\tau_2 = \frac{c}{a}\tau_1$, and further obtain $\tau_1 = \mu p_0$, when the strain in the adhesion zone is constant, i.e., we have:

$$\frac{\partial u_x}{\partial x} = -\frac{2\mu p_0 d}{aE^*} \tag{23}$$

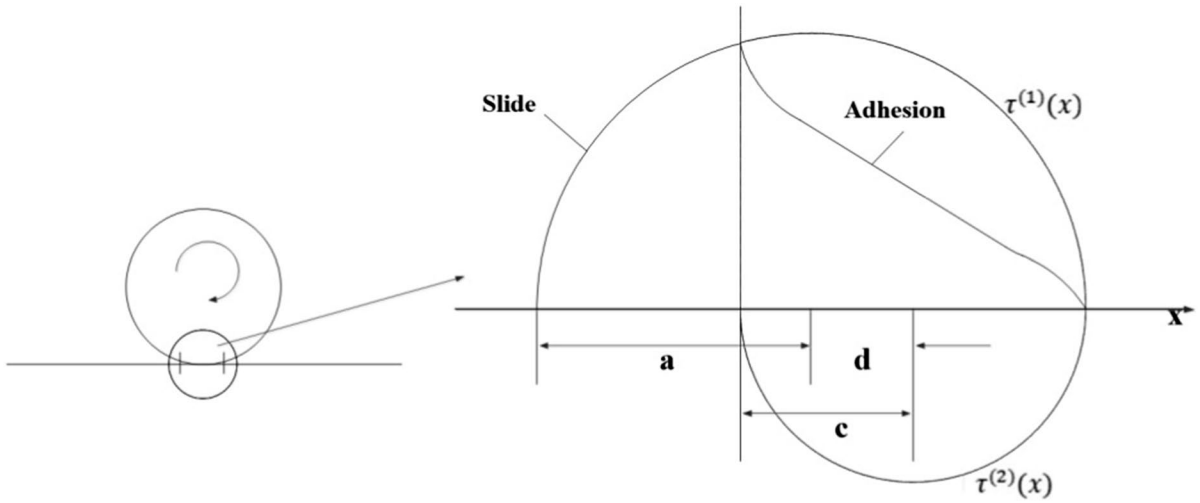

Fig. 9 Tangential stress distributions at the contact surface of the elastic wheel body in rolling contact

The total lateral force at the contact surface and the radius of the adhesion zone are:

$$F_x = \int_{-a}^{a} L\tau(x)dx = \left(\frac{\pi}{2}a\mu p_0 - \frac{c}{a}\frac{\pi}{2}c\mu p_0\right)L = \mu F_N\left(1 - \frac{c^2}{a^2}\right) \tag{24}$$

$$\frac{c}{a} = 1 - \frac{d}{a} = \left(1 - \frac{F_x}{\mu F_N}\right)^{\frac{1}{2}} \tag{25}$$

According to $s = \frac{\varepsilon_{xx}}{1+\varepsilon_{xx}} \approx \varepsilon_{xx}$ and $\frac{\partial u_x}{\partial x} = -\frac{2\mu p_0 d}{aE^*}$, the slip ratio can be obtained as:

$$s = \frac{\partial u_x}{\partial x} = -\frac{2\mu p_0}{E^*}\left[1 - \left(1 - \frac{F_x}{\mu F_N}\right)^{1/2}\right] \tag{26}$$

Consider these two relations $F_{\mathrm{N}} = \frac{\pi a p_0}{2}L$ and $F_{\mathrm{N}} = \frac{\pi E^* L a^2}{4R}$, then the slip ratio can be written in the form of.

$$s = -\frac{\mu a}{R}\left[1 - \sqrt{1 - \frac{F_x}{\mu F_N}}\right] \tag{27}$$

When $F_x = \mu F_{\mathrm{N}}$ the whole contact surface slides, it is known by Eq. (27) that the slipping ratio at this time is $s = -\frac{\mu a}{R}$ the maximum slip ratio is equal to the "elastic slip" under the same force. Thus, the maximum slip ratio is equal to the same force under the "elastic slip"$s \approx -\frac{aF_x}{2RF_{\mathrm{N}}}, F_x \ll \mu F_{\mathrm{N}}$ The difference between the two is 2 times: $s_{\mathrm{sliding}} = -\frac{\mu a}{2R}$. This is the partial slip caused by sliding, under the "critical traction" (the moment before the start of full sliding). The stress distribution on the contact surface is shown in Fig. 9.

The sliding speed in rolling contact is equal to: $v_{\mathrm{sliding}} \approx \frac{\mu a}{2R}v$. The traction force can be based on the expression for complete slip $s = -\frac{\mu a}{R}\left[1 - \sqrt{1 - \frac{F_x}{\mu F_{\mathrm{N}}}}\right]$ and the elastic partial slip expression $s \approx -\frac{aF_x}{2RF_{\mathrm{N}}}, F_x \ll \mu F_{\mathrm{N}}$ to estimate the difference between:

$$s_{\mathrm{sliding}} = -\frac{\mu a}{8R}\left(\frac{F_x}{\mu F_N}\right)^2 \tag{28}$$

According to the two requirements for rolling contact, the same conditions must be met as for cylindrical contact $\tau_2 = \frac{c}{a}\tau_1$ and $\tau_1 = \mu p_0$, then the strain and slip ratios are.

$$\frac{\partial u_x}{\partial x} = -\frac{\pi(4-3\nu)}{16G}\mu p_0\frac{d}{a} \tag{29}$$

The tangential forces and the radius of the adhesion zone are:

$$F_x = \frac{2}{3}\pi a^2\tau_1 - \frac{2}{3}\pi c^2\tau_2 = \mu F_{\mathrm{N}}\left[1 - \left(\frac{c}{a}\right)^3\right] \tag{30}$$

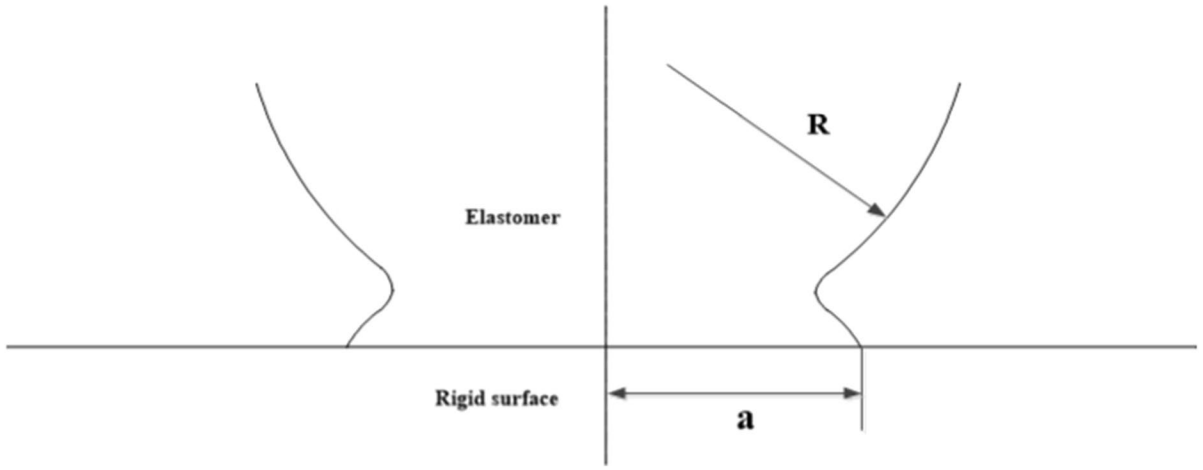

Fig. 10 Contact of highly elastic wheel body with rigid surface in rolling phase

$$\frac{c}{a} = \left(1 - \frac{F_x}{\mu F_N}\right)^{1/3} \tag{31}$$

Slippage ratio:

$$s = \frac{\partial u_x}{\partial x} = -\frac{3(4-3\nu)\mu F_N}{32Ga^2}\left[1 - \left(1 - \frac{F_x}{\mu F_N}\right)^{1/3}\right] \tag{32}$$

Transforming the slippage ratio gives a first-order approximation:

$$s \approx -\frac{(4-3\nu)F_x}{32Ga^2} \tag{33}$$

The equations are further combined to obtain the friction coefficient for elastic contact friction in the smooth rolling domain.

$$\mu = \frac{V_{\text{sliding}} 32Ga^2 3R}{(4-3\nu)V4E^* a^3\left[1 - \left(\frac{c}{a}\right)^3\right]} \tag{34}$$

In stage ⑤, which corresponds to the transitional rolling stage of elastic rolling contact friction in the discontinuous stage, the rubber wheel operates in a non-sliding pure rolling state when overcoming convex points. During this state, the high elastic material also experiences energy dissipation, which is known as resistance. The changes in the contact surface during the rolling stage are illustrated in Fig. 10.

The energy loss during rolling is estimated by treating the rolling as a "continuous reset" of the wheel, and for a sphere of radius R rolling on a rigid plane (contact radius a), the normal force F_{N} is.

$$F_{\text{N}} \approx \frac{4}{3}E^* R^{1/2} d^{3/2} \approx \frac{16}{3}G_\infty R^{1/2} d^{3/2} \tag{35}$$

where d is the indentation depth, and the estimated characteristic frequency is $\omega \approx \frac{v}{a}$, the strain amplitude is $\varepsilon_0 \approx \frac{d}{a}$, according to the energy dissipation of viscoelastic materials, the power loss per unit volume is obtained as.

$$\overline{P} = \frac{1}{2}\omega\varepsilon_0^2 G''(\omega) \approx \frac{1}{2}\frac{v}{a}\left(\frac{d}{a}\right)^2 G''\left(\frac{v}{a}\right) \tag{36}$$

The energy loss is $\dot{W} \approx 4vd^2 G''\left(\frac{v}{a}\right)$, and dividing the power by the velocity, we obtain the resistance as.

$$F_w \approx 4d^2 G''\left(\frac{v}{a}\right) \tag{37}$$

At low frequencies, the loss modulus is always proportional to the frequency, which can be expressed as $G''(\omega) = \overline{\eta}\omega$, where $\overline{\eta}$ is the dynamic viscosity at low frequencies, and then the resistance is.

$$F_w \approx 4\overline{\eta}\left(\frac{a^2}{R}\right)^2\left(\frac{v}{a}\right) = 4\overline{\eta}\frac{a^3}{R^2}v \tag{38}$$

By rewriting the above deformation volume and resistance equations through the Hertz final conclusion equation, the deformation volume is.

$$a^3 = \frac{3RF_N}{16G_\infty} \tag{39}$$

where G_∞ is the modulus of elasticity. For the resistance, there is: $F_w = F_N \frac{3}{4}\frac{v\tau}{R}$, then the rolling friction coefficient is.

$$\mu_{\text{rolling}} = \frac{F_w}{F_N} \approx \frac{3}{4}\frac{v\tau}{R} \tag{40}$$

where $\tau = \frac{\bar{\eta}}{G_\infty}$ is the relaxation time.

In stages ② to ⑥, there exists another type of friction in all microstates, which needs to consider the adhesion and hysteresis of the rubber material, i.e. the adhesion friction factor and the hysteresis friction factor. The viscoelastic property of rubber determines that rubber wheels are actually generally roll-slip motion, and the friction of tires moving on dry roads F_t the following formula can be applied to the calculation of.

$$F_t = F_a + F_h + F_m \tag{41}$$

where F_a is the sliding adhesion friction; F_h is the friction caused by hysteresis or deformation; F_m is the mechanical friction, including abrasion and rolling adhesion friction. The magnitude of the above three components are affected by temperature, sliding speed, physical properties of the material and surface area and its roughness. The cohesive friction factor and hysteresis friction factor are.

$$\mu_a = K_a \frac{1}{p^r} E'' \tag{42}$$

$$\mu_h = K_h \frac{E''}{E^{*2} p} \tag{43}$$

where K_a and K_h are constants; p is the normal force; the exponent $r = 0.2$; the E'' and E^* are the rubber loss and the composite modulus.

2.2.2 Elastic friction factor

In each stage, elastic contact friction can be broadly categorized into two types: elastic contact friction under the same surface motion state and elastic contact friction under the transitional motion state of discontinuous surfaces (Fig. 11).

Under the same surface motion state, both static friction and viscoelastic contact friction can be described. Static friction is defined by Eq. (9), while viscoelastic contact friction is represented by Eq. (44).

$$\mu_{all1} = K_a \frac{1}{p^r} E'' + K_h \frac{pE''}{E^{*2}} + \mu_0 \left(p/p_0\right)^{-1/3} \tag{44}$$

Elastic sliding contact friction and viscoelastic contact friction can be described using Eq. (45).

$$\mu_{all2} = \frac{1}{2}\tilde{\omega}\langle\sigma\rangle^2 \frac{G''(\tilde{\omega})}{|\hat{G}(\tilde{\omega})|^2} * \frac{\frac{\pi p_0}{4E^* a}\left(2a^2 - r^2\right)}{\frac{4}{3}E^* R^{\frac{1}{2}} d^{\frac{3}{2}}} + K_a \frac{1}{p^r} E'' + K_h \frac{pE''}{E^{*2}} \tag{45}$$

Viscoelastic contact friction and elastic rolling contact friction, specifically in the steady rolling domain, can be described by Eq. (46).

$$\mu_{all3} = K_a \frac{1}{p^r} E'' + K_h \frac{pE''}{E^{*2}} + \mu = \frac{V_{sliding} 32 G a^2 3R}{(4 - 3v) v 4E^* a^3 \left[1 - \left(\frac{c}{a}\right)^3\right]} \tag{46}$$

In the stage of discontinuous surfaces, the motion of the rubber wheel involves both viscoelastic contact friction and elastic rolling contact friction, specifically in the transitional rolling domain. During this stage, there is the formation of elastic rolling contact friction in the transitional rolling domain, accompanied by the adhesive and hysteresis effects on the rubber material itself. Therefore, in the context of elastic contact friction on discontinuous surfaces, the rubber wheel experiences both viscoelastic contact friction and elastic rolling contact friction, as described by Eq. (47).

$$\mu_{all4} = K_a \frac{1}{p^r} E'' + K_h \frac{pE''}{E^{*2}} + \frac{3}{4}\frac{v\tau}{R} \tag{47}$$

Based on the graphs illustrating the variations of the elastic friction factors in the five stages, it is evident that the comprehensive friction factors of each stage demonstrate nonlinear growth as the radial pretightening force increases. However, the elastic sliding contact friction stage and the elastic rolling friction stage (transitional rolling domain) experience the

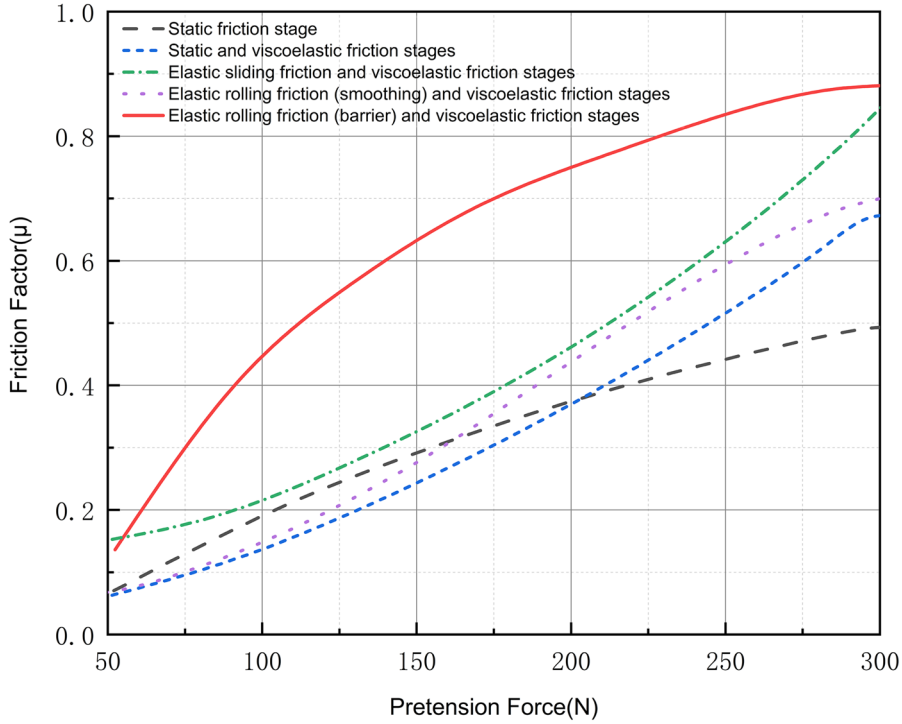

Fig. 11 Friction factor variation curve in each stage

states of starting and overcoming resistance, leading to more significant changes. This observation highlights the particular importance of radial pre-tightening force variations in these two stages, as they play a decisive role in facilitating effective inter-stage transitions in the variable-diameter internal drive device.

2.3 Radial preload analysis of the transition between stages of the variable diameter internal drive device

2.3.1 Mechanical correlation analysis

The magnitude of the radial pre-tightening force in the variable-diameter internal drive device, which unfolds on the inner wall of the sleeve, depends on several influential parameters of the structure itself. Thus, the calculation of the radial pre-tightening force is done using a specific formula. Initially, it is essential to consider the actual conditions of the radial pre-tightening force. During the unfolding process of the variable-diameter internal drive structure on the inner wall of the sleeve, the force applied to the rubber wheel differs between the steady state (same surface) and the transitional state (discontinuous surface). Consequently, the point of application of the radial pre-tightening force provided by the driving arm also varies accordingly. The steady state is illustrated in Fig. 12a.

The advancing shoe is pressed against the driving arm by the pre-tensioning push rod, and the thrust is then transmitted to the rubber wheel. Subsequently, the entire structure is compressed against the inner wall of the sleeve by the radial pre-tightening force, achieving a state of balance. The angle between the thrust provided by the pre-tensioning motor and the horizontal component of the driving arm is denoted as α. To ensure propulsion, the force state at this point is represented as $F_{p1} = \cos\alpha F_p$. The advancing shoe maintains its forward movement during this stage. The mechanical equilibrium at the rubber wheel is denoted as $F_q = F_{f2} + F_{gz}$ and $F_y = F_t + F_{z2}$. To determine the radial pre-tightening force at the rubber wheel, the thrust at the advancing plate is substituted into the mechanical equilibrium formula at the rubber wheel, resulting in $F_{p1}^2 = F_y^2 + F_q^2$, which is further calculated.

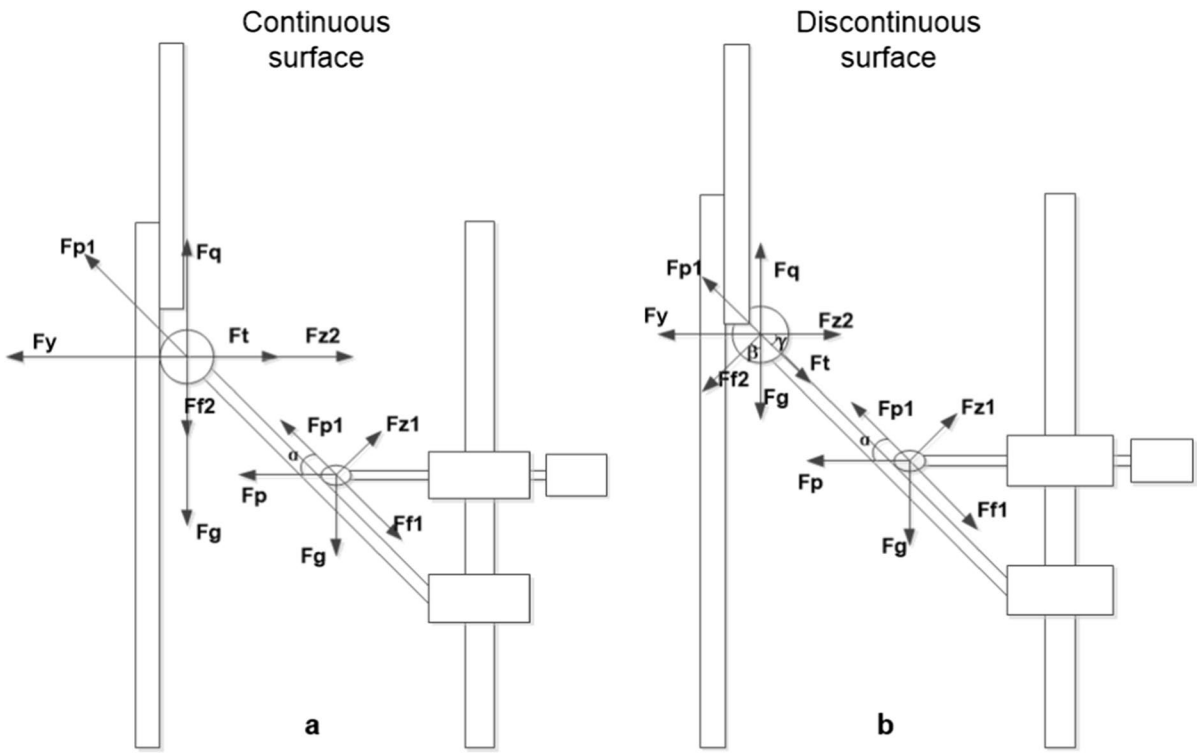

Fig. 12 Schematic diagrams of forces in steady state and transition state

$$\left(\cos\alpha F_p\right)^2 = F_y^2 + \left(F_{f2} + F_{gz}\right)^2 \tag{48}$$

The total weight at this point is the sum of all physical weights, excluding the central column and the inner wall of the sleeve.

$$F_{f2} = \mu\left(F_y - F_t - F_{z2}\right) \tag{49}$$

Radial preload in equilibrium:

$$F_y = \sqrt{\left(\cos\alpha F_p\right)^2 - \left(\mu\left(F_y - F_t - F_{z2}\right) + F_{gz}\right)^2} \tag{50}$$

The transitional state, as shown in Fig. 12b, is characterized by the dependence of radial pre-tightening force variation on the rotational angle. The calculation process is as follows: The magnitude of the frictional force is determined by the angle β, which represents the inclination between the horizontal direction at the contact point of the rubber wheel and the vertical force on the discontinuous surface. The elastic force acts in the opposite direction to the thrust provided by the advancing plate, with its angle of variation γ gradually decreasing relative to the horizontal support force. The calculation of radial pre-tightening force in the transitional state is outlined below.

$$F_y^2 = \left(\cos\alpha F_p\right)^2 - \left(F_{f2}\cos\beta + F_{gz}\right)^2 \tag{51}$$

$$F_{f2} = \left(F_y - F_t - F_{z2}\right)\mu \tag{52}$$

The elasticity at this point is based on the angle of clamping γ obtained:

$$F_{f2} = \left(F_y - F_t\cos\gamma - F_{z2}\right)\mu \tag{53}$$

Hence, the radial pre-tightening force in the ultimate transitional state is:

$$F_y = \sqrt{\left(\cos\alpha F_p\right)^2 - \left(\left(F_y - F_t\cos\gamma - F_{z2}\right)\mu\cos\beta + F_{gz}\right)^2} \tag{54}$$

It is important to note that the variable-diameter internal drive device experiences zero gravity when it is in space orbit. Therefore, in this case, the factor F_{gz} is not considered.

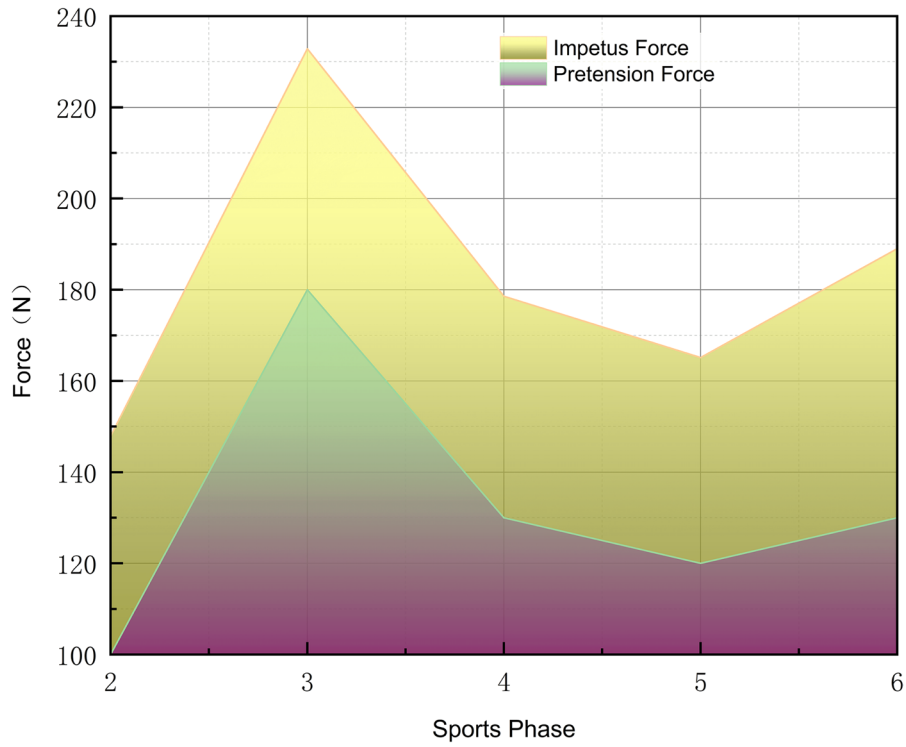

Fig. 13 Variation curve of radial preload versus thrust force provided by the preload assembly

2.3.2 *Radial preload output analysis*

The friction coefficient calculation formula that accounts for the radial pre-tightening force in both the same surface state and the discontinuous surface state can be derived by substituting the normal force and radial pre-tightening force into the friction coefficient expression and including the relevant variables affecting the radial pre-tightening force. Specifically, for static friction:

$$\mu = \mu_0 \left(\sqrt{\left(\cos \alpha F_p\right)^2 - \left(\mu\left(F_y - F_t - F_{z2}\right) + F_{gz}\right)^2} / p_0 \right)^{-1/3} \tag{55}$$

By applying the same approach, the radial pre-tightening force formula (50) should be substituted into formulas (44), (45), and (46) individually. Furthermore, during the transition phase between non-contiguous surface levels, the radial pre-tightening force formula (54) in the transitional state should be substituted into formula (47). The variation curve illustrating the relationship between the radial pre-tightening load and the thrust generated by the pre-tensioning motor under a load of 60N is presented in Fig. 13. It is important to note that the friction coefficients remain consistent throughout each stage.

The figure reveals a complete transition of the radial pre-tightening force between levels, necessitating 5 adjustments. These adjustments correspond to different stages of friction contact and enhance the stability of contact during the transition phase between levels. The maximum radial pre-tightening force reaches 180N. Furthermore, during the transition state, the radial pre-tightening force exhibits a trend of decreasing to increasing, aligning with the structural motion.

Table 1 Test data of each movement phase

	Movement speed (mm/s)	Radial preload (N)	Elastic wheel embedment depth (mm)
Stage 2	4.8206	38.6421	3.5557
Stage 3	4.0791	34.6373	3.2844
Stage 4	5.8134	32.0228	3.1646
Stage 5	6.6029	43.2857	4.3584
Stage 6	7.8109	39.6113	3.5859

3 Finite element analysis of inter-stage transitions

3.1 Elastic contact friction analysis

To investigate the elastic contact friction at different stages of the radial-variable internal drive device during level transition, the finite element analysis method is utilized. Specifically, the analysis focuses on examining the elastic contact friction between the rubber wheel and the inner wall of the sleeve metal. In order to proceed with the analysis, it is essential to first define and establish all the materials and boundary conditions within the model.

Currently, due to the rapid development of various technologies in the aviation field, spatial structures are equipped with temperature control systems. This advancement enables the application of temperature-restricted materials in aviation. In order to validate the effectiveness of the variable diameter internal drive device and the accuracy of the related theory in transitioning non-continuous surfaces of the sleeve, we have selected materials similar to the variable diameter preload device used on the ground. The structural components are made of 2A12, which possesses high tensile and yield strength, as well as good machinability. The pin-shaft is made of 40Cr, known for its wear resistance and high load capacity. For the gear, we utilize 45CrNiMoV, military-grade low-alloy ultrahigh-strength steel with exceptional strength. The spring is made of 60Si2MnA, which exhibits comprehensive mechanical properties after undergoing heat treatment. As for the driving wheel, it is constructed from a rubber material that demonstrates wear resistance, stable performance under various conditions, and a certain level of impact resistance. In this study, nitrile rubber is specifically chosen due to its advantages over other synthetic rubbers, particularly when sulfurized with white carbon black, enhancing its comprehensive performance.

In the process of setting the boundary conditions for the model, several steps are followed. Firstly, the bottom end of the sleeve is fixed with constraints, ensuring stability while allowing freedom of movement for the rubber wheel. This freedom enables the occurrence of tangential slippage, which is influenced by the radial preload force acting on the rubber wheel. Furthermore, standard indoor temperature and humidity are established. Since the model will be deployed in orbit, the influence of gravity acceleration is disregarded, considering its negligible effect. The sleeve is positioned axially, and specific values for the rotational speed and radial preload force of the rubber wheel are determined. Finally, the contact modes between various components of the model are defined, along with the identification of the types of friction that occur during contact. To facilitate observation and focus on key elements, the cloud diagram exclusively displays the inner wall of the sleeve and the rubber wheel.

Figure 14 illustrates the complete elastic contact and friction states of the rubber wheel on the non-continuous surface during the transition stages. The contact states are represented by letters: a for the contact state during static friction and viscoelastic friction loading in stage ③, b for the contact state during sliding friction and viscoelastic friction loading in stage ④, c for the contact state during rolling friction and viscoelastic friction loading in stage ⑤, and d for the contact state during sliding friction and viscoelastic friction loading in stage ⑥, considering different radial preload forces. Examining the contact states, it is evident that the contact area is larger during the stages of static friction and sliding friction when compared to the rolling friction stage (transition stage). The respective areas are 4.47 mm^2, 3.84 mm^2, and 2.06 mm^2. As the rubber wheel transitions to stage ⑥, the contact area, shown in Fig. 14d, measures 3.71 mm^2. This difference is attributed to variations in radial preload force caused by different diameters and loads under the same state, resulting in distinct contact areas between the rubber and metal.

The friction forces in each stage show a non-linear increase with the rise of radial preload force, as evidenced by the data obtained from the elastic contact and friction state cloud diagrams of stages ③ to ⑥. Moreover, the changes in contact of the rubber wheel align with the corresponding motion states depicted in Fig. 5.

The friction force and radial preload force variation curves for stages ③ to ⑥ were obtained by analyzing the relationship between friction stress data in the elastic contact state and the radial preload force function, as illustrated in Fig. 15. When the same radial preload force is applied, the friction force follows the order: stage ④ > stage ⑤ > stage ⑥. This indicates that, within the same transition stage, the friction force in sliding friction is greater than that in rolling friction, and the friction force

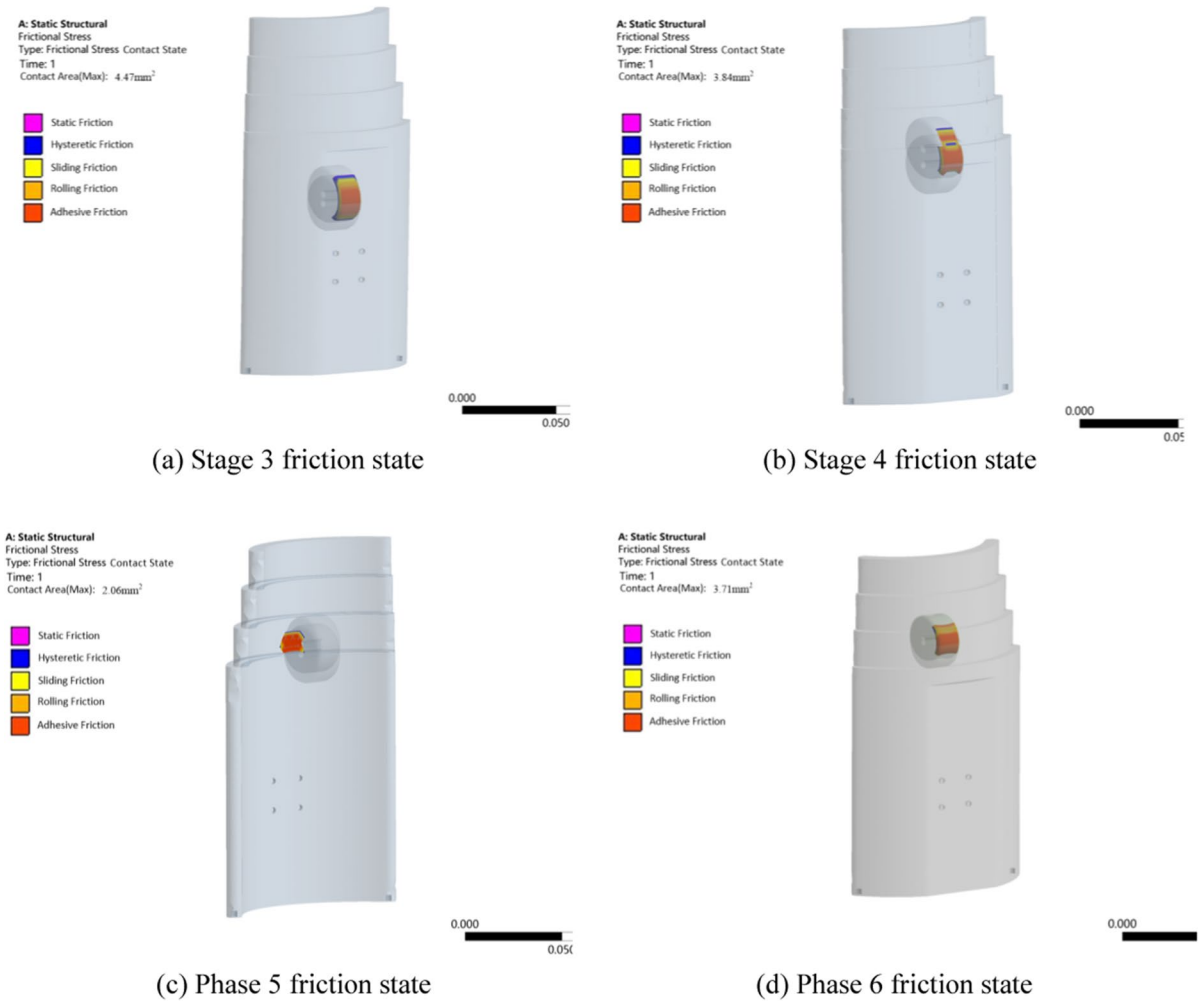

Fig. 14 Frictional contact clouds for each stage

gradually decreases as the transition stages differ. The decrease in friction force can be attributed to the formation of a "forceful" model between the driving arm and the preload plate component as the sleeve diameter gradually decreases, leading to a reduction in the contact area. To ensure effective contact, it is necessary to adjust the magnitude of the radial preload force in accordance with the thrust provided by the preload plate component, as depicted in Fig. 13. This adjustment helps to increase the elastic contact area, enhance friction, and ensure a smooth transition between stages.

3.2 Elastic contact-kinematic analysis

To validate the output state of the radial pre-tension load at each stage, we utilized the ADAMS virtual prototype method to simulate the progressive unfolding process of the structure. This process is depicted in Fig. 16.

Boundary conditions were established as follows: the global ambient temperature was set to 23 °C. The connections and contacts between components were achieved using rigid-flexible coupling surfaces. Individual contact was ensured between the elastic wheel, driving arm, sleeve at each stage, transmission components, and pre-tensioning components. Boolean operations were applied to the

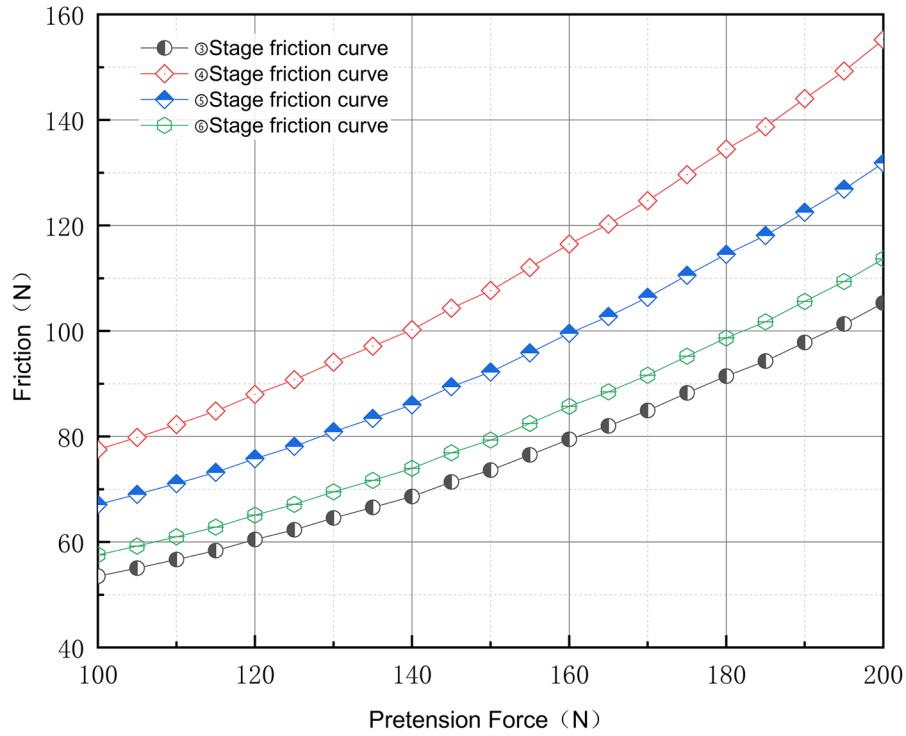

Fig. 15 Friction-radial preload force relationship graph

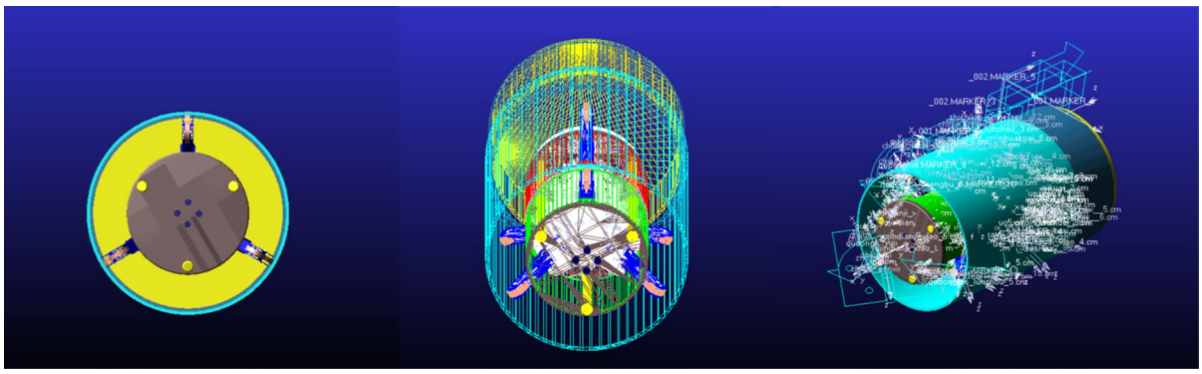

Fig. 16 ADAMS prototype model

remaining components. Slip joints, rotational joints, fixed joints, and friction joints were employed, with corresponding driving forces applied to the slip and rotational joints. The motor torque specified in Sect. 3.1 was transmitted through the transmission components to drive the elastic wheel. The same pre-tension load was applied. Aluminum alloy and butadiene rubber were selected as the materials. Flexible iterative solvers and automatic deformation control methods were utilized.

As shown in Fig. 17a, peaks in the rotational speed variation of the variable-diameter internal drive device during inter-stage transitions on the discontinuous surface can be observed. This phenomenon may result from the collision between the elastic wheel and the discontinuous surface due to velocity. During the time interval of 0.6–1.2 s, the elastic wheel's velocity decreases from 6 to 4.8 mm/s due to the influence of the radial pre-tightening load, accompanied by a decrease in the

(a) Rubber wheel movement speed

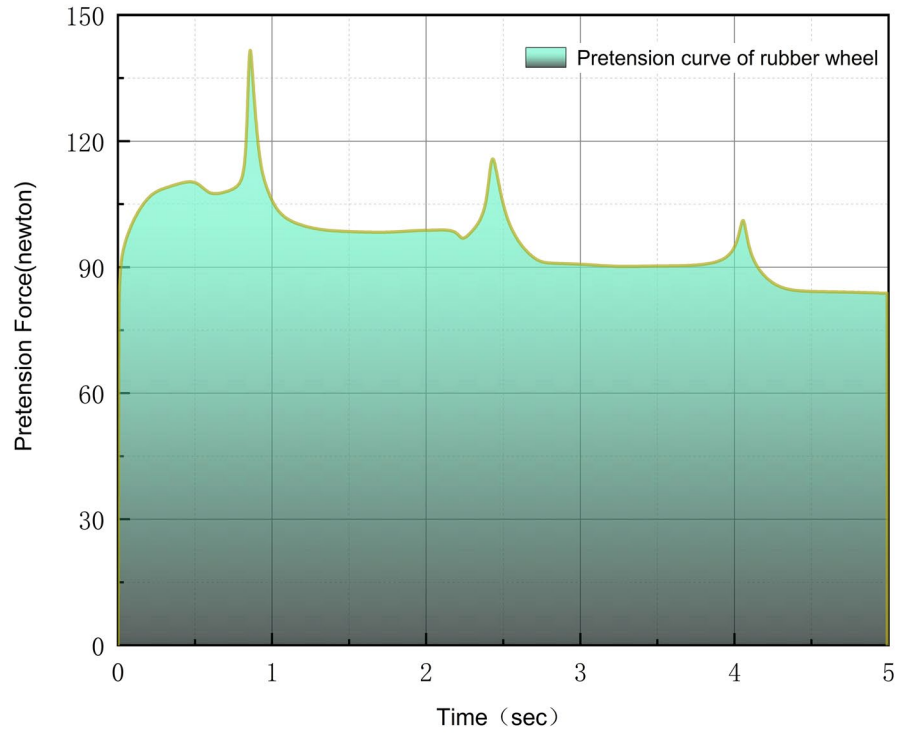

(b) Variation of preload force on rubber wheel

Fig. 17 Rotational speed variation curve and radial preload output curve

transition diameter. Subsequently, as a result of the rebound phenomenon caused by elastic collision, the elastic wheel undergoes freewheeling, reaching a maximum velocity of 7.9 mm/s. However, due to the radial pre-tightening load, the elastic wheel comes into contact with the discontinuous surface again, resulting in a velocity decrease to 5.1 mm/s. Figure 17a illustrates the velocity variation during one inter-stage transition phase. The current focus is primarily on expansion, which involves reducing the velocity and carefully observing the inter-stage transition under low-speed conditions. Specifically, under low-speed conditions with a load of 60N, Fig. 17b presents the output situation of the radial pre-tightening load at each stage.

Figure 17b illustrates the complete three-stage inter-stage transition deployment process, where three effective adjustments of radial pre-tightening load occur at moments 1 s, 2.5 s, and 4 s during each inter-stage transition. As the sleeve diameter decreases, the top load also decreases, resulting in peak radial pre-tightening forces of 150N, 118.4N, and 96.3N, respectively. The decreasing changes can be attributed to the different elastic contact friction states at each stage, as well as the variations in sleeve diameter and load across different stages. While the overall trend indicates a gradual decrease in the required radial pre-tightening load for maintaining axial advancement, there are instances where the radial pre-tightening force during the inter-stage transition phase exceeds that of the previous stage. This phenomenon arises due to the disparities in elastic contact friction types and structural moments between different stages.

The output of radial pre-tightening forces at each stage, as depicted in Fig. 17b, is consistent with the results of theoretical research and aligns with the radial pre-tightening force variation trend presented in Fig. 11. Furthermore, considering the radial pre-tightening force's significance as a key parameter influencing the elastic friction coefficient at each stage, it provides further evidence that the elastic friction coefficients at different stages in the simulation correspond to the findings of theoretical research. In the experimental section, a comparative graph illustrating the friction coefficient curves at each stage under theoretical, simulation, and experimental conditions will be included.

4 Experimental results and discussion

To validate the accuracy of the mathematical model and simulation analysis concerning the elastic contact friction theory and the radial preload load of the variable-diameter internal drive device during the transition between non-contiguous surface levels, we designed and fabricated a test prototype specifically for conducting elastic contact friction tests and discussions during the level transition of the variable-diameter internal drive device. The variable-diameter internal drive device is a centrally axisymmetric structure comprising six identical variable-diameter drive components. For the purpose of this study, we selected one of these components, representing 1/6th of the complete variable-diameter internal drive device, to serve as the test prototype. It is essential to note that the dimensional parameters of the test prototype's variable-diameter drive component maintain a 1:1 ratio with the corresponding component of the complete variable-diameter internal drive device. Additionally, the material selection for the test prototype aligns with that used in the theoretical and simulation stages. To ensure consistent boundary conditions as in the simulation stage, we had to make adjustments to the positions of the drive motor and the preload motor. This required recalculating the traction force on the wheel and the radial preload force in the theoretical state and verifying the output values.

In Fig. 18, the test prototype can be observed to be composed of two main sections: the sleeve support section and the variable-diameter drive pre-tensioning section. The purpose of the sleeve support section is to provide geometric constraints to the variable-diameter drive pre-tensioning section, allowing it to move axially along the inner wall surface of the sleeve. The sleeve support section comprises several components, namely the base, sleeve local structure, back support, and central pillar. The distance between the central pillar and the maximum outer diameter of the sleeve local structure measures 150 mm. The central pillar has a height of 215 mm, while the sleeve local structure's height is 280 mm, with each level separated by a radius of 4 mm. On the other hand, the variable-diameter drive pre-tensioning section serves the purpose of supplying the axial driving force and radial pre-tensioning force for the rubber wheel. This section

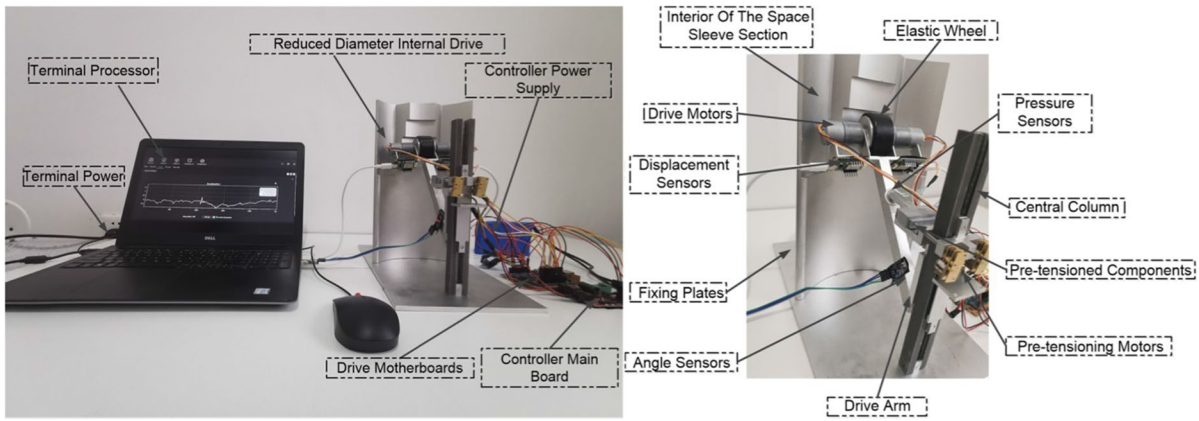

Fig. 18 Test prototype and sensor acquisition points

includes various components such as the rubber wheel itself, the drive arm, sliding connector, pre-tensioning component, and motor assembly. The rubber wheel has a radius of 25 mm and a width of 28 mm, while the drive arm measures 145 mm in length with a cross-section of 12*15 mm. The pre-tensioning component can elongate from 12 to 35 mm, and the sliding connector allows for an axial displacement of 85 mm.

Speed sensors, displacement sensors, pressure sensors, and angle sensors were strategically positioned on the test prototype to capture crucial data such as the movement speed of the rubber wheel, the compression amount of the rubber wheel (which can be converted into the contact area between materials), and the tangent value of the rubber wheel's displacement angle. To ensure the experiment's accuracy and relevance to real-world scenarios, a 60N load was applied to the variable-diameter internal drive device. This load allowed us to assess the elastic contact friction status at each stage during the transition of the variable-diameter internal drive device on the non-contiguous surface inside the sleeve. The primary objectives of these measurements were to obtain the friction coefficient variation curve at each stage of elastic contact friction, providing valuable insights into the device's performance and behavior during the transition process.

Figures 19 and 20 display the test data curves for the motion speed and pre-tensioning force, respectively, with consistent pre-tensioning force output and driving speed states. Each set of experiments was conducted 40 times, resulting in four average curves depicted in Figs. 19 and 20.

Throughout the complete unfolding process, the motion speed experiences variations at different stages of level transition. The four average curves presented in the figure are obtained by fitting the average data from every 10 motion data acquisitions. Notably, each curve exhibits a similar trend. Following the initial transition, to maintain motion speed consistency at each level, the motion speed decreases as the spatial sleeve diameter decreases. Remarkably, the figure illustrates that during each level transition, the velocity curve displays peaks and valleys.

Figure 20 displays the fitted curve, representing the average of the data collected from 40 sets of experiments. Since the variable-diameter internal drive device is a double-layer symmetric structure, each layer contains independent structures with an angle of 120 degrees. For analysis purposes, we focused on a completed 1/6 symmetric structure of the entire design, with one layer of symmetric structure illustrated in Fig. 17b. Consequently, the data in Fig. 20 accounts for 1/3 of the complete simulation results, based on the pre-tensioning force output outcomes. Observing the figure, it becomes apparent that the radial pre-tensioning force diminishes as the spatial sleeve diameter decreases. Additionally, during the level transition phase, there are peaks and valleys in the pre-tensioning force. Combining this observation with the analysis from Fig. 19, it is evident that the change in pre-tensioning force during different stages of level transition leads to variations in motion speed. Moreover, we obtained the data curve of the elastic

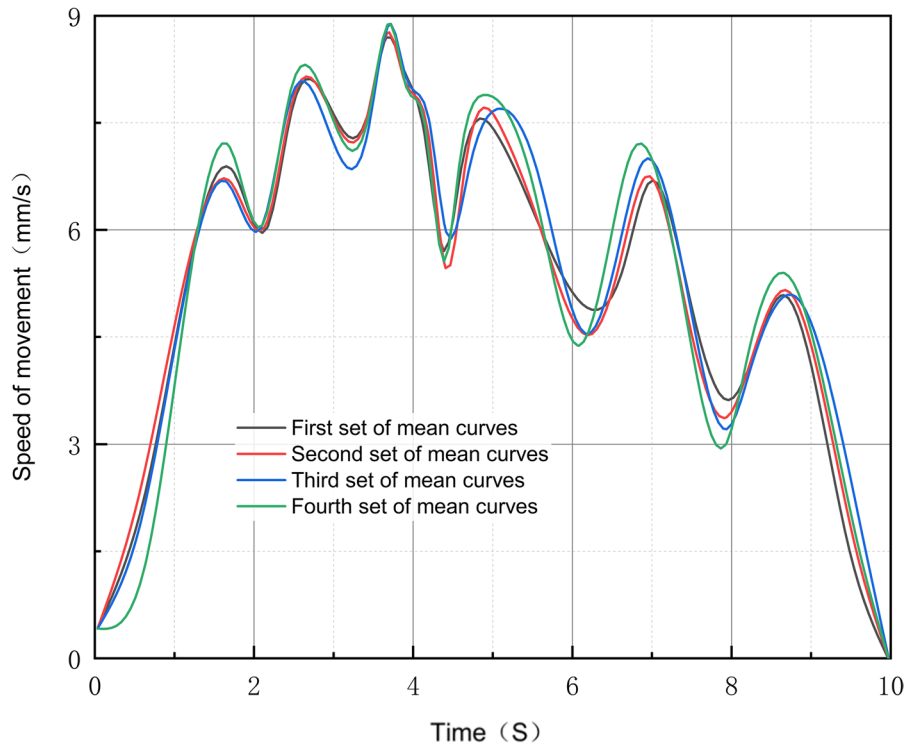

Fig. 19 Speed test data curve

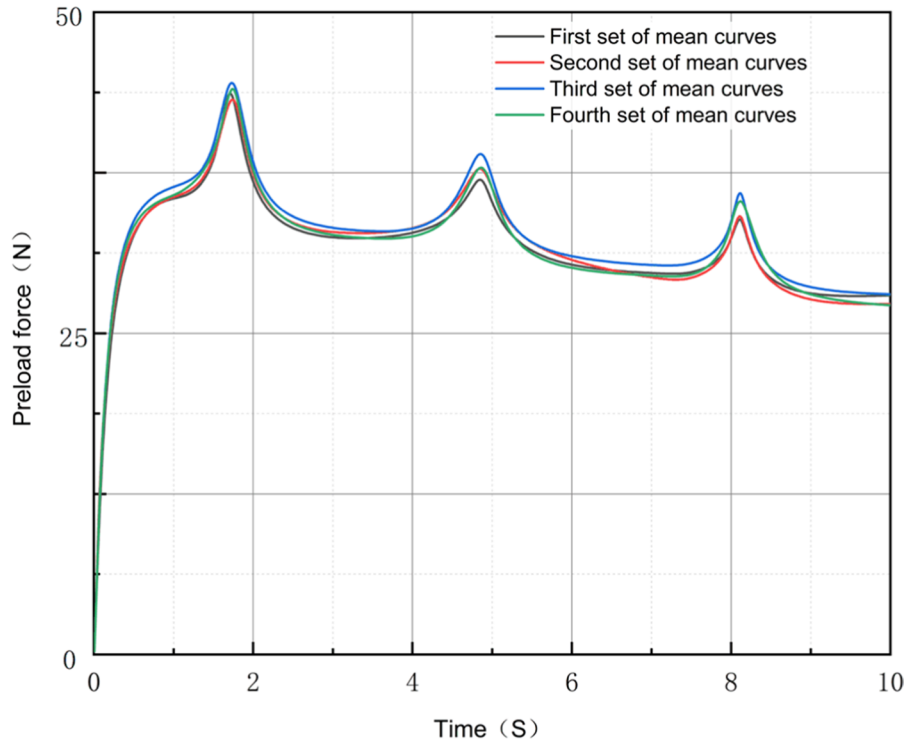

Fig. 20 Preload test data curve

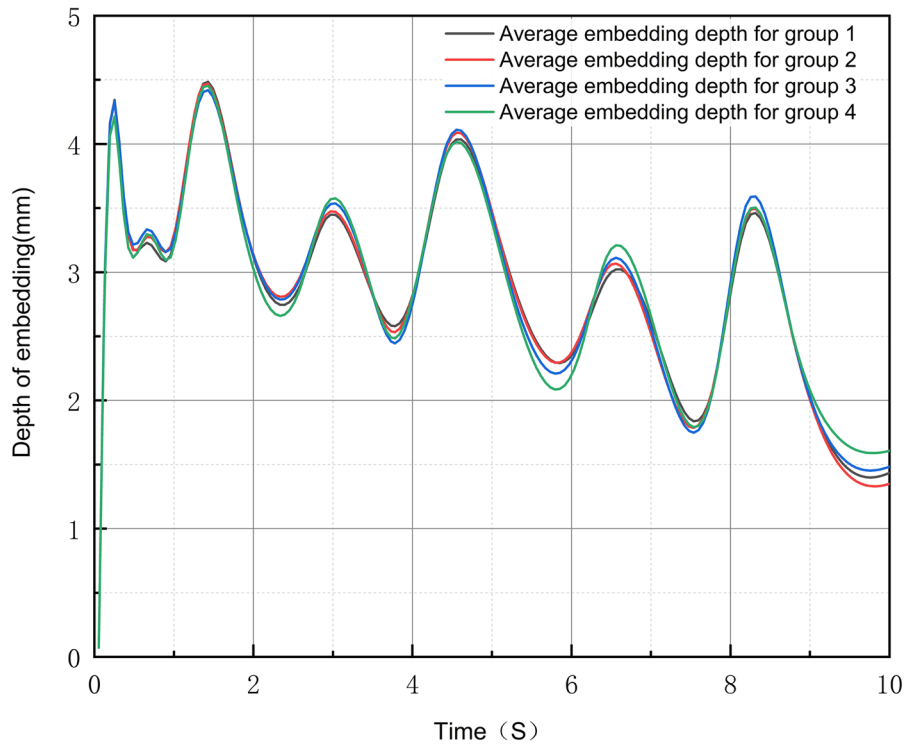

Fig. 21 Elastic wheel embedding depth data curve

wheel embedding depth in the above two states, as shown in Fig. 21.

Figure 21 provides valuable insights into the behavior of the elastic wheel during different stages of level transition, as it undergoes varying degrees of embedding under the combined influence of motion speed and radial pre-tensioning force. The changes in embedding depth correspond to the motion state of the variable-diameter internal drive device within the spatial sleeve. Notably, during each level transition, the embedding depth gradually decreases with the reduction of pre-tensioning force and speed. For a comprehensive overview, Table 1 presents the extreme values of motion speed, radial pre-tensioning force, and embedding depth for each motion stage.

Using the experimental data from each motion stage as presented in Table 1, friction force curves were derived for each stage by employing the elastic contact friction theory model. Figure 22 illustrates the variation curve between the radial pre-tensioning force and the friction force at each stage during the complete operation of the variable-diameter internal drive device.

From Fig. 22, it is evident that the variation between the radial pre-tensioning force and the friction force at each stage corresponds to the motion state of the variable-diameter internal drive device during the level transition, thereby validating the effective transition of the variable-diameter internal drive device on the non-contiguous surface inside the sleeve. Examining the variations in friction force at each stage, the friction force in the fourth stage is greater than that in the fifth stage, followed by the sixth stage, and then the third stage. A comparison with Fig. 15, which depicts the friction force and radial pre-tensioning force variation curve during the simulation stage, reveals that the experimental data at the same pre-tensioning force output stage is slightly smaller than the simulation data. This difference is attributed to the machining errors of the experimental components.

Figure 23 illustrates the fitting curves of the friction coefficients at different stages for the theoretical state, simulation state, and experimental state. Observing the fitting curves of the friction coefficients at different stages under these three states, it becomes evident that the comprehensive friction factors for each stage exhibit nonlinear growth. Upon analyzing the data collected from the experiments, it was found that the fitting curves of the friction

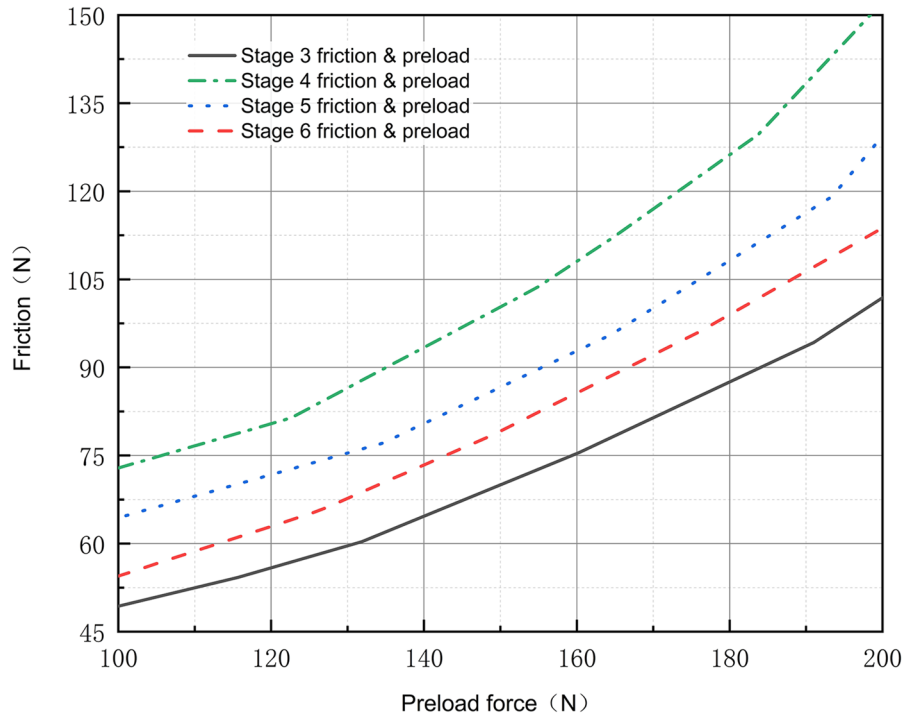

Fig. 22 Variation curve between radial preload force and friction force at each stage

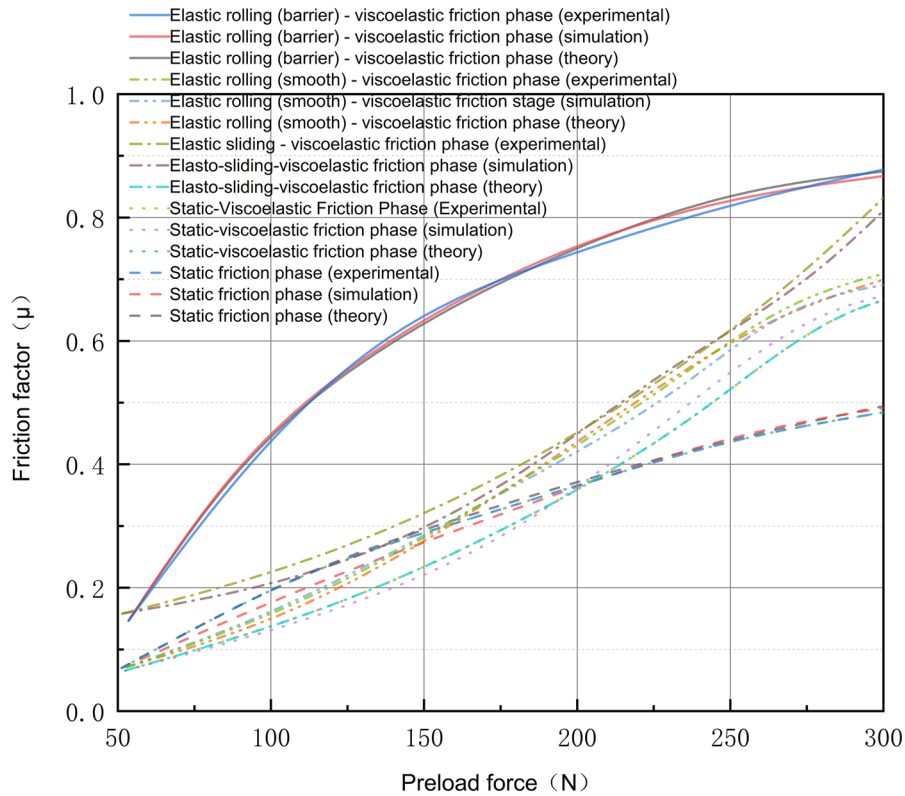

Fig. 23 Friction factor fitting curves for different stages of the three states

coefficients closely resemble those of the theoretical and simulation states, with more pronounced variations in the elastic sliding friction stage and elastic rolling friction stage (transitional rolling domain). However, when compared to the other two states, the data curve for the experimental state shows a slight decrease. This decrease is attributed to rubber wear and external environmental factors resulting from multiple experiments.

In summary, the experimental results indicate a correlation between the elastic contact friction state and the variation of the friction coefficient during the level transition of the variable-diameter internal drive device on the non-contiguous surface inside the sleeve. The findings, when combined with the theoretical model, clearly show that the change in the friction coefficient is influenced not only by the pre-tensioning force but also by the contact area between the viscoelastic material and the metal material.

5 Conclusions

Currently, the mismatch between the contact friction state of the viscoelastic material and the output of the radial pre-tightening force hinders effective inter-stage transitions of the variable-diameter internal drive device on non-continuous surfaces inside the sleeve, resulting in issues such as jamming, slipping, and sliding. To address this, this paper focuses on analyzing and establishing a theoretical model that explores the relationship between elastic contact friction and radial pre-tightening force during inter-stage transitions on non-continuous surfaces, using the variable-diameter internal drive device as the subject. The validity of the theory is assessed through the analysis of simulation prototypes and the production of principle prototypes, ultimately confirming the effectiveness of the proposed inter-stage transition theory.

Firstly, we investigate the elastic contact friction at each stage of the variable-diameter internal drive device during inter-stage transitions. We establish different models for elastic contact friction under various motion conditions to obtain the friction coefficient variation curves for each stage. By utilizing the analytical relationship between radial pre-tightening force and friction force, we adjust the contact area between the rubber wheel and the metal surface through the radial pre-tightening force. This adjustment allows for effective transitions of the variable-diameter internal drive device on non-continuous surfaces by modifying the friction coefficient. Subsequently, we analyze the effects of radial pre-tightening force, external load, and material contact area on inter-stage transitions using finite element method and virtual prototyping techniques. This analysis leads to the determination of relationship curves between friction force and radial pre-tightening force at different stages during inter-stage transitions. Finally, we design and fabricate a 1:1 scale experimental prototype to validate the influence of the contact area between radial pre-tightening force and different materials on the friction coefficient at each stage.

Due to limitations in knowledge and time, this study primarily focused on the theoretical research and experimental verification of the elastic contact friction theory during inter-stage transitions of the variable-diameter internal drive device. However, it is important to note that this work is preliminary, and there are areas for future investigation. Specifically, the analysis of inter-stage transitions has only considered the influence of radial pre-tightening force on the elastic contact friction of the rubber wheel after applying radial force. Nevertheless, the impact of collision and the resulting asynchronous structural unfolding process when the rubber wheel contacts the non-continuous surface at higher motion rates has not been taken into account. This aspect will be a key area of research in future studies.

Acknowledgements This work was supported by the National Natural Science Foundation of China, No. 12073028 (Study of Variable diameter internal drive device/Passive Locking High Stiffness Deployment Technology for Deployable Very Large Aperture Space Telescope).

Declarations

Conflict of interest The authors declare that they have no knowledge of competing financial interests or personal relationships that may have influenced the work reported herein.

References

1. Mettler E, Breckenridge WG, Quadrelli MB (2020) Large aperture space telescopes in formation: modeling, metrology, and control. J Astronaut Sci 53:391–412. https://doi.org/10.1007/BF03546360

2. Shaolin Lu, Qi X, Ying Hu, Li B, Zhang J (2019) Deployment dynamics of large space antenna and supporting arms. IEEE Access 7:69922–69935. https://doi.org/10.1109/access.2019.2918614
3. Liu G, Chen W, Wang W, Chen Y (2016) Design and analysis of a novel space deployable mechanism of ring and frustum type. Int J Adv Manuf Technol 94(9):3251–3264. https://doi.org/10.1007/s00170-016-9472-9
4. Li Q, Liu L, Shen J (2020) One novel distributed space telescope with payload formation. IEEE Access 8:13949–13957. https://doi.org/10.1109/access.2020.2965581
5. Sun Z, Yang D, Duan B, Kong L, Zhang Y (2021) Structural design, dynamic analysis, and verification test of a novel double-ring deployable truss for mesh antennas. Mech Mach Theory 165:104416. https://doi.org/10.1016/j.mechmachtheory.2021.104416
6. Cheng P, Ding H, Cao W-a, Gosselin C, Geng M (2020) A novel family of umbrella-shaped deployable mechanisms constructed by multi-layer and multi-loop spatial linkage units. Mech Mach Theory 161:104169. https://doi.org/10.1016/j.mechmachtheory.2020.104169
7. Zhao Na, Luo Y, Wang G, Shen Y (2022) A deployable articulated mechanism enabled in-flight morphing aerial gripper. Mech Mach Theory 167:104518. https://doi.org/10.1016/j.mechmachtheory.2021.104518
8. Liu S, Li Q, Wang P, Guo F (2020) Kinematic and static analysis of a novel tensegrity robot. Mech Mach Theory 149:103788. https://doi.org/10.1016/j.mechmachtheory.2020.103788
9. Yi Yang Hu, Liu HZ, Peng Y, Yushu Yu (2021) Two types of remote-center-of-motion deployable manipulators with dual scissor-like mechanisms. Mech Mach Theory 160:10427. https://doi.org/10.1016/j.mechmachtheory.2021.104274
10. Guo J, Zhao Y, Yundou Xu, Zhang G (2022) Mechanics analysis and structural design of a truss deployable antenna mechanism based on 3RR-3URU tetrahedral unit. Mech Mach Theory 171:104749. https://doi.org/10.1016/j.mechmachtheory.2022.104749
11. Guo J, Zhao Y, Zhang G, Liu E, Liu B, Yundou Xu (2022) Configuration synthesis and unfolding stiffness characteristics analysis of a truss antenna connecting mechanism based on URU-RR-URU hexagonal deployable unit. Mech Mach Theory 177:105047. https://doi.org/10.1016/j.mechmachtheory.2022.105047
12. Zhang G, He J, Guo J, Xia X (2022) Dynamic modeling and vibration characteristics analysis of parallel antenna. Mech Sci 13(2):1019–1029. https://doi.org/10.5194/ms-13-1019-2022
13. BoWen Zhong (2008) The design and analysis of telescope mast. Dissertation, Harbin Instituteof Technology
14. Mobrem M, Spier C (2012) Design and performance of the telescopic tubular mast. US Government Technology Report, pp 1–14.
15. Cao N, Zhang X, Li Z (2017) Deployable boom for sunshield structure of large space telescope. Acad J Manuf Eng 15(4):34–41
16. Sofla MS, Sadigh MJ, Zareinejad M (2021) Design and dynamic modeling of a continuum and compliant manipulator with large workspace. Mech Mach Theory 164:10441. https://doi.org/10.1016/j.mechmachtheory.2021.104413
17. Zhang Z, Tang S, Fan W, Xun Y, Wang H, Chen G (2022) Design and analysis of hybrid-driven origami continuum robots with extensible and stiffness-tunable sections. Mech Mach Theory 169:104607. https://doi.org/10.1016/j.mechmachtheory.2021.104607
18. Malm CG, Davids WG, Peterson ML, Turne AW (2009) Experimental characterization and finite element analysis of inflated fabric beams. Constr Build Mater 23(5):2027–2034. https://doi.org/10.1016/j.conbuildmat.2008.08.029
19. Wagner P, Wriggers P, Veltmaat L, Clasen H, Prange C, Wies B (2017) Numerical multiscale modelling and experimental validation of low speed rubber friction on rough road surfaces including hysteretic and adhesive effects. Tribol Int 111:243–253. https://doi.org/10.1016/j.triboint.2017.03.015
20. De Lorenzis L, Wriggers P (2013) Computational homogenization of rubber friction on rough rigid surfaces. Comput Mater Sci 77:264–280. https://doi.org/10.1016/j.commatsci.2013.04.049
21. Fangman Xu, Yoshimura K-I, Mizuta H (2013) Experimental study on friction properties of rubber material: influence of surface roughness on sliding friction. Proc Eng 68:19–23. https://doi.org/10.1016/j.proeng.2013.12.141
22. Liang XM, Xing YZ, Li LT, Yuan WK, Wang GF (2021) An experimental study on the relation between friction force and real contact area. Sci Rep 11:20366. https://doi.org/10.1038/s41598-021-99909-2
23. Popov VL, Dimaki A, Psakhie S, Popov M (2015) On the role of scales in contact mechanics and friction between elastomers and randomly rough self-affine surfaces. Sci Rep 5:11139. https://doi.org/10.1038/srep11139